CrossMark

The Regulation of the Solar Wind Electron Heat Flux by Wave–Particle Interactions

Jesse T. Coburn[1,2] , Daniel Verscharen[1] , Christopher J. Owen[1] , Milan Maksimovic[3] , Timothy S. Horbury[4] ,
Christopher H. K. Chen[5] , Fan Guo[6] , Xiangrong Fu[6,7] , Jingting Liu[1] , Joel B. Abraham[1] , Georgios Nicolaou[1] ,
Maria Elena Innocenti[8] , Alfredo Micera[8] , and Vamsee Krishna Jagarlamudi[9]

[1] Mullard Space Science Laboratory, University College London, Dorking RH5 6NT, UK
[2] Space Science Institute, Boulder, CO 80301, USA
[3] LESIA, Observatoire de Paris, Université PSL, CNRS, Sorbonne Université, Université de Paris, 5 Place Jules Janssen, F-92195 Meudon, France
[4] The Blackett Laboratory, Imperial College London, London, SW7 2AZ, UK
[5] Department of Physics and Astronomy, Queen Mary University of London, London, E1 4NS, UK
[6] Los Alamos National Laboratory, Los Alamos, NM 87545, USA
[7] New Mexico Consortium, Los Alamos, NM 87544, USA
[8] Institut für Theoretische Physik, Ruhr-Universität Bochum, Bochum, Germany
[9] Applied Physics Laboratory, Johns Hopkins University, Laurel, MD 20723, USA

Abstract

The solar wind electrons carry a significant heat flux into the heliosphere. The weakly collisional state of the solar wind implicates collisionless processes as the primary factor that constrains nonthermal features of the velocity distribution function (VDF), including the heat flux. Previous observational work suggests that the electron VDF sometimes becomes unstable to the whistler wave, but reliance on model VDFs (e.g., drifting bi-Maxwellians) has proven insufficient for an exact description of the behavior of the solar wind electrons—in particular, the regulation of the heat flux. The characterization of these processes requires methods to obtain fine details of the VDF and quantification of the impact of kinetic processes on the VDF. We employ measurements of the electron VDF by Solar Orbiter's Solar Wind Analyser and of the magnetic field by the Radio and Plasma Waves instrument to study an unstable solar wind electron configuration. Through a Hermite–Laguerre expansion of the VDF, we implement a low-pass filter in velocity space to remove velocity space noise and obtain a VDF suitable for analysis. With our method, we directly measure the instability growth rate and the rate of change of the electron heat flux through wave–particle interactions.

1. Introduction

The solar wind plasma consists of protons, electrons, and a small concentration of heavier ions, all of which are rarely in local thermodynamic equilibrium due to relatively small collision frequencies (Marsch 2006; Verscharen et al. 2019). Measurements of the solar wind electron velocity distribution function (VDF) display a majority population (∼90%) called the core population that is quasi-Maxwellian, and three non-Maxwellian features: (i) the strahl population—a superthermal field-aligned beam; (ii) the halo population—quasi-isotropic superthermal electrons; (iii) and the deficit—a lack of electrons typically on the sunward side of the VDF (Feldman et al. 1975; Marsch 2006; Halekas et al. 2020; Owen et al. 2022; Salem et al. 2023). The electrons contribute to the solar wind energetics in two major ways: the divergence of their heat flux contributes directly to the total thermal energy budget, and the gradient of their pressure supports an ambipolar electric field that contributes to the acceleration of the solar wind.

The heat flux is an important source of thermal energy density for the overall solar wind energy budget, in particular in the slow solar wind (Štverák et al. 2015; Abraham et al. 2022). The heat flux is regulated by a combination of Coulomb collisions, which are more efficient at low particle energies, and by collisionless processes such as kinetic instabilities

(Hollweg 1974; Gary et al. 1975; Scudder 1992; Gary et al. 1994; Scime et al. 1994; Gary et al. 1999; Salem et al. 2003; Bale et al. 2013; Štverák et al. 2015). The regulation of the heat flux by kinetic instabilities is a well-studied topic, but incomplete theory—because a simple (e.g., density and temperature) description is not sufficient to describe the multitude of coupled thresholds (Gary et al. 1999; Lazar et al. 2017, 2018; Micera et al. 2021; Verscharen et al. 2022)—prompting nonmodel VDF descriptions of plasma instabilities (Astfalk & Jenko 2017; Verscharen et al. 2018). The relative effectiveness of collisional and kinetic processes is tied to large-scale variations (e.g., in the density or magnetic field), as well as energy deposition by the turbulent electromagnetic fields, complicating a complete description of electron heat flux regulation.

Exospheric models attribute the acceleration of the protons to an ambipolar electric field caused by the high mobility of the superthermal electrons in the collisionless solar wind. The description interprets features in the electron VDF as signatures of solar wind acceleration (Jockers 1970; Pierrard & Lemaire 1996; Maksimovic et al. 1997; Landi & Pantellini 2003; Scudder 2019; Berčič et al. 2021a). The ambipolar electric field results in a finite-potential well for electrons: the high-energy electron population is able to escape the well, and lower-energy electrons undergo electrostatic reflection. The escaping population does not return to repopulate the sunward side of the electron VDF, resulting in a decrease in the phase space density on the sunward side (Jockers 1970; Landi et al. 2012). This asymmetry, called a deficit or cutoff in energy, is

set by the escape energy of electrons in the potential well, and it has been measured to empirically estimate the contribution of the ambipolar potential to the acceleration of the solar wind (Berčić et al. 2020; Halekas et al. 2020; Berčić et al. 2021a; Halekas et al. 2023). As an asymmetry in the local VDF, the deficit contributes to the heat flux in the near-Sun region (Halekas et al. 2020, 2023).

To better understand how the electrons contribute to the global solar wind, through both the ambipolar potential and the heat flux, a firm understanding of the regulation of non-Maxwellian features due to instabilities must be established. Our study builds upon a recent observation by Berčić et al. (2021b) of whistler waves that are generated by the deficit. We determine the unstable feature of the electron VDF by measuring the wave growth rate and quantifying the rate at which the macroscopic moments change. In particular, we measure the rate of change of the electron heat flux due to the generation of whistler waves.

2. Quasilinear Theory

Quasilinear theory is a framework to study the evolution of the background VDF through resonant emission and absorption of plasma waves (Shapiro & Shevchenko 1964; Kennel 1966; Yoon 2017). The theory assumes that the background VDF evolves on a slower timescale than the wave period and that the damping/growth rate is small compared to the wave frequency (Stix 1992). The equations describe the evolution of the background VDF as a diffusion of phase space density self-consistently with the evolution of the wave energy spectrum.

In Section 2.1, we introduce the quasilinear equations, and in Section 2.2 we produce the rate of change of the moments (e.g., change in momentum, temperature, and heat flux).

2.1. Definitions and Equations

Following Marsch & Tu (2001) and Marsch (2006), the background VDF (F_s) evolves as

$$\frac{\partial}{\partial t}F_s(t, v_\parallel, v_\perp) = \frac{1}{(2\pi)^3}\int d^3k \ \hat{\mathcal{B}}(\boldsymbol{k}) \ \times \ \frac{1}{v_\perp}\frac{\partial}{\partial\alpha}v_\perp\nu_s(\boldsymbol{k}, v_\parallel, v_\perp)\frac{\partial}{\partial\alpha}F_s(t, v_\parallel, v_\perp),\tag{1}$$

where t is the time variable, the subscript "s" denotes the species, $v_\parallel$ ($v_\perp$) is the parallel (perpendicular) velocity with respect to the magnetic field direction, and $\boldsymbol{k}$ is the wavevector, with $k_\parallel$ ($k_\perp$) being the component parallel (perpendicular) to the magnetic field direction. The definition of the wave-frame pitch-angle gradient is

$$\frac{\partial}{\partial\alpha} = v_\perp\frac{\partial}{\partial v_\parallel} + (v_{\text{phase}}(\boldsymbol{k}) - v_\parallel)\frac{\partial}{\partial v_\perp},\tag{2}$$

where the phase speed is $v_{\text{phase}}(\boldsymbol{k}) = \omega(\boldsymbol{k})/k_\parallel$ and α is the wave-frame pitch angle. The complex frequency is $\tilde{\omega}(\boldsymbol{k}) = \omega(\boldsymbol{k}) + i\gamma(\boldsymbol{k})$, where $\omega(\boldsymbol{k})$ is the real part and $\gamma(\boldsymbol{k})$ is the imaginary part. In Equation (1), the normalized magnetic field energy spectrum

$$\hat{\mathcal{B}}(\boldsymbol{k}) = 8\pi\frac{\mathcal{B}(\boldsymbol{k})}{|\boldsymbol{B}_0|^2}\left(\frac{k_\parallel}{|\boldsymbol{k}|}\right)^2\frac{1}{1 - |\hat{\boldsymbol{k}}\cdot\boldsymbol{e}(\boldsymbol{k})|^2},\tag{3}$$

where $\boldsymbol{B}_0$ is the background field and $\hat{\boldsymbol{k}} = \boldsymbol{k}/|\boldsymbol{k}|$ is the unit wavevector. The following definitions of the magnetic field $\boldsymbol{B}(t, \boldsymbol{x})$ complete the definition of the magnetic field energy spectrum:

$$\mathcal{B}(\boldsymbol{k}) = \frac{|\tilde{\boldsymbol{B}}(\boldsymbol{k})|^2}{8\pi V},\tag{4}$$

$$\boldsymbol{B}(t, \boldsymbol{x}) = \int d^3k \ \tilde{\boldsymbol{B}}(\boldsymbol{k}) \ e^{i\boldsymbol{k}\cdot\boldsymbol{x}} \ e^{-i\int_0^t dt' \ \tilde{\omega}(t',\boldsymbol{k})},\tag{5}$$

$$\tilde{\boldsymbol{B}}(\boldsymbol{k}) = \frac{1}{(2\pi)^3}\int d^3x \ \boldsymbol{B}(t, \boldsymbol{x}) \ e^{-i\boldsymbol{k}\cdot\boldsymbol{x}} \ e^{i\int_0^t dt' \ \tilde{\omega}(t',\boldsymbol{k})},\tag{6}$$

where V is the integrating volume of $\boldsymbol{x}$, defining the bounds for the integral in $\boldsymbol{x}$ and $\boldsymbol{k}$. The time integral in the exponential can be simplified as $\int_0^t dt' \ \tilde{\omega}(t', \boldsymbol{k}) \to \omega(\boldsymbol{k}) \, t$, using the method of unperturbed orbits (Gary 1993). The polarization vector $\boldsymbol{e}(\boldsymbol{k})$ is defined according to Stix (1992) such that $\omega(\boldsymbol{k})$ is positive and the wave polarization changes with the sign of $k_\parallel$. Moreover, the definition of the scattering rate is

$$\nu_s(\boldsymbol{k}, v_\parallel, v_\perp) = \pi\frac{\Omega_s^2}{|k_\parallel|}\sum_{p=-\infty}^{\infty}\delta(V_s(\boldsymbol{k}, p) - v_\parallel)$$
$$\left|\frac{1}{2}\left[J_{p-1}\left(\frac{k_\perp v_\perp}{\Omega_s}\right)e^+ + J_{p+1}\left(\frac{k_\perp v_\perp}{\Omega_s}\right)e^-\right] + \frac{v_\parallel}{v_\perp}J_p\left(\frac{k_\perp v_\perp}{\Omega_s}\right)e^z\right|^2,\tag{7}$$

where $\Omega_s = q_s|\boldsymbol{B}_0|/m_s c$ is the cyclotron frequency, q_s is the elementary charge, m_s is the mass, c is the speed of light, and $J_p(k_\perp v_\perp/\Omega_s)$ is the Bessel functions of the first kind. The resonant speed is

$$V_s(\boldsymbol{k}, p) = \frac{\omega(\boldsymbol{k}) - p \, \Omega_s}{k_\parallel},\tag{8}$$

where p is the order of the resonance. Finally, the polarization vectors are

$$e^\pm(\boldsymbol{k}) = e^x(\boldsymbol{k}) \pm ie^y(\boldsymbol{k}),\tag{9}$$

where the "+" is for left-handed circular, "−" is for right-handed circular, and $e^z(\boldsymbol{k})$ is for longitudinal polarization. The magnetic field power spectrum evolves as

$$\frac{\partial}{\partial t}\mathcal{B}(\boldsymbol{k}) = 2\gamma(\boldsymbol{k})\mathcal{B}(\boldsymbol{k}).\tag{10}$$

The solution to the dielectric tensor, the wave energy equation (Equation (10)), and the time-evolution equation of the background VDF (Equation (1)) form the set of quasilinear equations.

2.2. Moments of the Quasilinear Equations

The velocity moments of Equation (1) lead to the rate of change of the moments under the action of quasilinear diffusion

(Marsch & Tu 2001). Following Appendix A, we find

$$\frac{1}{n_s}\frac{\partial}{\partial t}\begin{pmatrix} n_s u_\parallel^s \\ p_\parallel^s \\ p_\perp^s \\ q_\parallel^s \\ q_\perp^s \end{pmatrix}$$

$$= \frac{\Omega_s^2}{(2\pi)^3}\int_{-\infty}^{\infty} d^3k\; \hat{\mathcal{B}}(\boldsymbol{k})\frac{1}{k_\parallel}\sum_{p=-\infty}^{\infty}\int_0^{\infty} dv_\perp\; \mathcal{R}_s(\boldsymbol{k}, p)$$

$$\times \begin{pmatrix} 1 \\ 2m_s V_s'(\boldsymbol{k}, p) \\ \dfrac{pm_s\Omega_s}{k_\parallel} \\ 3m_s V_s'(\boldsymbol{k}, p)^2 \\ \dfrac{m_s}{2}\left(v_\perp^2 + 2V_s'(\boldsymbol{k}, p)\dfrac{p\Omega_s}{k_\parallel}\right) \end{pmatrix} + \begin{pmatrix} 0 \\ 0 \\ 0 \\ -3\dfrac{p_\parallel^s}{n_s}\dfrac{\partial u_\parallel^s}{\partial t} \\ -\dfrac{p_\perp^s}{n_s}\dfrac{\partial u_\parallel^s}{\partial t} \end{pmatrix}, \qquad (11)$$

where the resonance function[10] is

$$\mathcal{R}_s(\boldsymbol{k}, p)$$
$$= -\frac{k_\parallel}{|k_\parallel|}2\pi^2\left| \frac{v_\perp}{2}\left[J_{p-1}\left(\frac{k_\perp v_\perp}{\Omega_s}\right)e^+ + J_{p+1}\left(\frac{k_\perp v_\perp}{\Omega_s}\right)e^- \right]\right.$$
$$\left. + V_s(\boldsymbol{k}, p)J_p\left(\frac{k_\perp v_\perp}{\Omega_s}\right)e^z \right|^2 \left(\frac{\partial}{\partial\alpha}F_s(t, v_\parallel, v_\perp)\right)_{v_\parallel = V_s(\boldsymbol{k}, p)}. \qquad (12)$$

The definition of the plasma-frame resonant speed is

$$V_s'(\boldsymbol{k}, p) = \frac{\omega(\boldsymbol{k}) - p\,\Omega_s}{k_\parallel} - u_\parallel^s, \qquad (13)$$

where $u_\parallel^s$ is the parallel bulk velocity. The remaining moments are

$$n_s = 2\pi\int_{-\infty}^{\infty} dv_\parallel \int_0^{\infty} dv_\perp\, v_\perp\, F_s(t, v_\parallel, v_\perp), \qquad (14a)$$

$$n_s u_\parallel^s = 2\pi\int_{-\infty}^{\infty} dv_\parallel \int_0^{\infty} dv_\perp\, v_\perp\, v_\parallel\, F_s(t, v_\parallel, v_\perp), \qquad (14b)$$

$$p_\parallel^s = 2\pi\int_{-\infty}^{\infty} dv_\parallel \int_0^{\infty} dv_\perp\, v_\perp\, m_s(v_\parallel - u_\parallel^s)^2\, F_s(t, v_\parallel, v_\perp), \qquad (14c)$$

$$p_\perp^s = 2\pi\int_{-\infty}^{\infty} dv_\parallel \int_0^{\infty} dv_\perp\, v_\perp\, \frac{m_s}{2}v_\perp^2\, F_s(t, v_\parallel, v_\perp), \qquad (14d)$$

$$q_\parallel^s = 2\pi\int_{-\infty}^{\infty} dv_\parallel \int_0^{\infty} dv_\perp\, v_\perp\, m_s(v_\parallel - u_\parallel^s)^3\, F_s(t, v_\parallel, v_\perp), \qquad (14e)$$

$$q_\perp^s = 2\pi\int_{-\infty}^{\infty} dv_\parallel \int_0^{\infty} dv_\perp\, v_\perp\, \frac{m_s}{2}(v_\parallel - u_\parallel^s)\, v_\perp^2\, F_s(t, v_\parallel, v_\perp). \qquad (14f)$$

The moments define the number density n_s, the parallel pressure $p_\parallel^s$, the perpendicular pressure $p_\perp^s$, the parallel heat flux $q_\parallel^s$, and the perpendicular heat flux $q_\perp^s$ of species "s."

---

[10] Integrating the resonance function over $v_\perp$ recovers the definition of Marsch & Tu (2001) and Marsch (2006), but their definition does not generalize to the perpendicular heat flux, due to the $v_\perp^2$ dependence in the first large parentheses on the right-hand side of Equation (11).

3. Measurements and Analysis

3.1. Observations

Measurements for this study are made by the Solar Orbiter spacecraft, which is a European Space Agency mission dedicated to establishing how the Sun creates and controls the heliosphere (Müller et al. 2020). Solar Orbiter's Solar Wind Analyser/Electron Analyser System (SWA/EAS), Radio and Plasma Waves (RPW) instrument, and magnetic field instrument (MAG) provide the data set of this study. SWA/EAS measures solar wind electrons in the energy range of a few eV up to 5 keV, providing the three-dimensional VDF (Owen et al. 2020). This study uses the burst-mode data product from SWA/EAS, which provides a reduced gyrotropic VDF covering the full pitch-angle span at a time cadence of 0.125 s (Owen et al. 2021). The RPW instrument is designed to measure the electric field in the low-frequency range from <1 vector s^{-1} up to 10^3 vectors s^{-1} and the magnetic field with 10–10^3 vectors s^{-1}, as well as high-frequency ranges for both fields (Maksimovic et al. 2020). The MAG instrument measures the vector magnetic field at a frequency of 16 vectors s^{-1} in normal mode and up to 128 vectors s^{-1} in burst mode (Horbury et al. 2020).

We apply the moment-based quasilinear theory to the same interval studied by Berčič et al. (2021b). A summary of the key findings is reported here:

1. Observations on 2020 June 24 show a narrowband enhancement of magnetic fluctuations that are coincident with a non-Maxwellian electron VDF.
2. The enhancement is between the proton and electron cyclotron frequencies, exhibiting propagation features quasi-parallel to the magnetic field (the angle relative to the background magnetic field is 3.8°), and the wave ellipticity of the magnetic enhancement is >0.5, being consistent with quasi-parallel right-hand circularly polarized whistler waves.
3. The electron VDF is skewed in the parallel direction by the presence of the strahl and deficit.
4. The cyclotron-resonance condition (Equation (8)) for whistler waves maps the peak frequency of the magnetic field power spectrum to the deficit region of the electron VDF.

3.2. Data Analysis

The primary observations that lead to a measurement of the rate of change (see Equation (11)) of the moments are the magnetic field energy spectrum and the wave-frame pitch-angle gradient of the electron VDF. The analysis of the electron VDF involves four steps:

1. Interpolate the electron VDF from instrument coordinates to the Hermite–Laguerre quadrature points in parallel–perpendicular velocity space.
2. Take the Hermite–Laguerre transform to obtain spectral coefficients.
3. Truncate the spectral coefficients to obtain a noiseless VDF.
4. Use the Hermite–Laguerre recursion relations to obtain gradients, e.g., $\partial F_e/\partial\alpha$.

The description of the Hermite and Laguerre polynomials is in Appendix B. These steps provide a noiseless and trustworthy VDF, as well as the velocity space gradients of the VDF, which
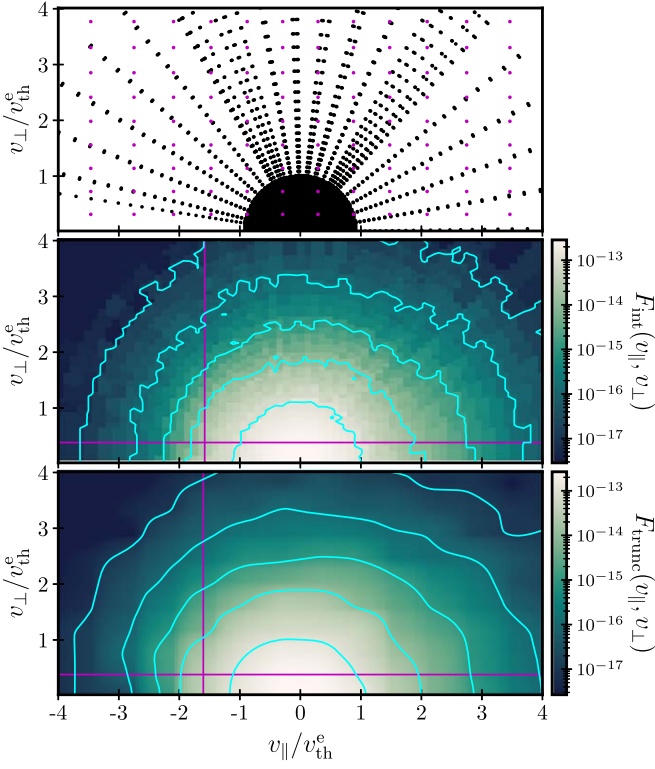
Figure 1. The horizontal (vertical) axis is the parallel (perpendicular) velocity normalized by v_{th}^e. The top panel displays the SWA/EAS coordinates as black dots, where the black region, near the origin, is the portion of the electron VDF < 15 eV. The magenta dots show the Hermite–Laguerre quadrature points. The middle panel is the result of the interpolation from the instrument coordinates to the Hermite–Laguerre quadrature points. The bottom panel is the result of the Hermite–Laguerre method. Both the middle and bottom panels are normalized so they integrate to unity. The magenta lines (in the middle and bottom panels) mark cuts through the VDF that are plotted in Figure 3. The cyan lines are contours of the normalized VDF at the levels (10^{-17}, 10^{-16}, 10^{-15}...).

we use for our analysis. In the final section of the data analysis (Section 3.6), we compute the rate of change of the macroscopic variables according to Equation (11).

3.3. Interpolation of the Electron VDF from Spacecraft Coordinates to Hermite–Laguerre Quadrature

The average of the electron VDF over an 8 s window, coinciding with the RPW magnetic field snapshot waveform, provides the background VDF. We remove the energy <15 eV portion of the VDF, because it is contaminated by spacecraft electrons, and repopulate it by extrapolating a Maxwellian fit from the remaining core electrons (i.e., energies between 15 and 60 eV). The background VDF must be transformed from SWA coordinates (energy, azimuth, elevation) to cylindrical coordinates using $v_\parallel = \hat{\boldsymbol{b}} \cdot \boldsymbol{v}$, $v_\perp = |\boldsymbol{v} - \hat{\boldsymbol{b}} \cdot \boldsymbol{v}|$, where $\hat{\boldsymbol{b}} = \boldsymbol{B}_0/|\boldsymbol{B}_0|$.

The top panel of Figure 1 displays the transformed SWA/EAS coordinates (SWA/EAS instrument coordinates) as black dots, where the black region near the origin shows the range of energies (<15 eV) contaminated by spacecraft electrons. The new points, which are the Hermite–Laguerre quadrature points, appear as magenta dots. The number of points for the new grid is 60 in each dimension; see Section 3.4 for further justification. We plot the result of the interpolation ($F_{int}(v_\parallel, v_\perp)$) from native coordinates to the new coordinates in the middle panel of

Figure 1. The function $F_{int}(v_\parallel, v_\perp)$ contains a structure that is a mixture of instrumental noise, interpolation noise, and kinetic physics.

We normalize the velocity space coordinates by the thermal velocity $v_{th}^e = \sqrt{2k_B T_e/m_e}$, where we measure the electron temperature by computing the moments in Equations (14a) and use $p_e = n_e k_B T_e$. The moments appear in Table 1. All the anisotropic quantities (e.g., T_e, p_e, and q_e) relate to the total as $T_e = T_\parallel^e/3 + 2T_\perp^e/3$. We do not separate the core and halo; the core and halo parameters are provided by Berčič et al. (2021b). The region of $v_\parallel = [-4v_{th}^e, -2v_{th}^e]$ exhibits a lower VDF than $v_\parallel = [2v_{th}^e, 4v_{th}^e]$. This is due to the field-aligned strahl ($v_\parallel > 0$) and the sunward deficit ($v_\parallel < 0$).

3.4. Hermite–Laguerre Expansion

Our analysis technique calculates the expansion of the electron VDF with the Hermite ($\psi_m(\hat{v}_\parallel)$) and Laguerre ($\Gamma_l^n(\hat{v}_\perp)$) functions on their respective quadrature. The quadrature permits exact integrals for Hermite–Laguerre polynomials of order $2n - 1$, where n is the order of the largest polynomial considered.

The expansion of the VDF is

$$F_{int}(v_\parallel, v_\perp) \approx \sum_{m,l=0}^{M,L} c_{ml} \, \psi_m(\hat{v}_\parallel) \, \Gamma_l^0(\hat{v}_\perp), \tag{15}$$

where M, L are the maximum orders of the Hermite–Laguerre polynomials, c_{ml} are the Hermite–Laguerre spectral coefficients, and the arguments are $\hat{v}_\parallel = v_\parallel/v_{th,e}^\parallel$, $\hat{v}_\perp = v_\perp/v_{th,e}^\perp$. The thermal velocities are therefore requirements for which we use the moments of the VDF (see Table 1). The orthonormality conditions of the Hermite–Laguerre functions permit the calculation of the spectral coefficients,

$$c_{ml} \approx \int_{\mathcal{A}(v_\parallel)} dv_\parallel \int_{\mathcal{A}(v_\perp)} dv_\perp \, \psi_m(\hat{v}_\parallel) \, \Gamma_l^0(\hat{v}_\perp) F_{int}(v_\parallel, v_\perp), \tag{16}$$

where $\mathcal{A}(v_\parallel)$, $\mathcal{A}(v_\perp)$ are the bounds set by the Hermite–Laguerre quadrature points.

Figure 2 presents the spectral coefficients from Equation (16). The top panel is the two-dimensional Hermite–Laguerre spectrum normalized to c_{00}^2, and the bottom panel presents line plots of the spectral coefficients. The largest spectral coefficient is c_{00}^2, which confirms the choice of the basis function, in particular that $v_{th,e}^\perp$, $v_{th,e}^\parallel$ are an appropriate representation of the data for the purpose of the Hermite–Laguerre expansion. The spectral coefficients decrease in relative strength until $m, l \approx 14$ where the spectrum flattens. We interpret this flattening as the characteristic noise floor. The Hermite spectral coefficients display more power in the even orders than the odd orders, reflecting zeroth-order symmetry about $v_\parallel$, yet the spectral coefficients of odd order are not zero, capturing asymmetric features, e.g., strahl and deficit. We determine the number of new grid points (magenta points in the left panel of Figure 1) by increasing it until the low orders of the spectrum (seen in Figure 2) are no longer altered; we find the number at which this occurs to be 60 points.
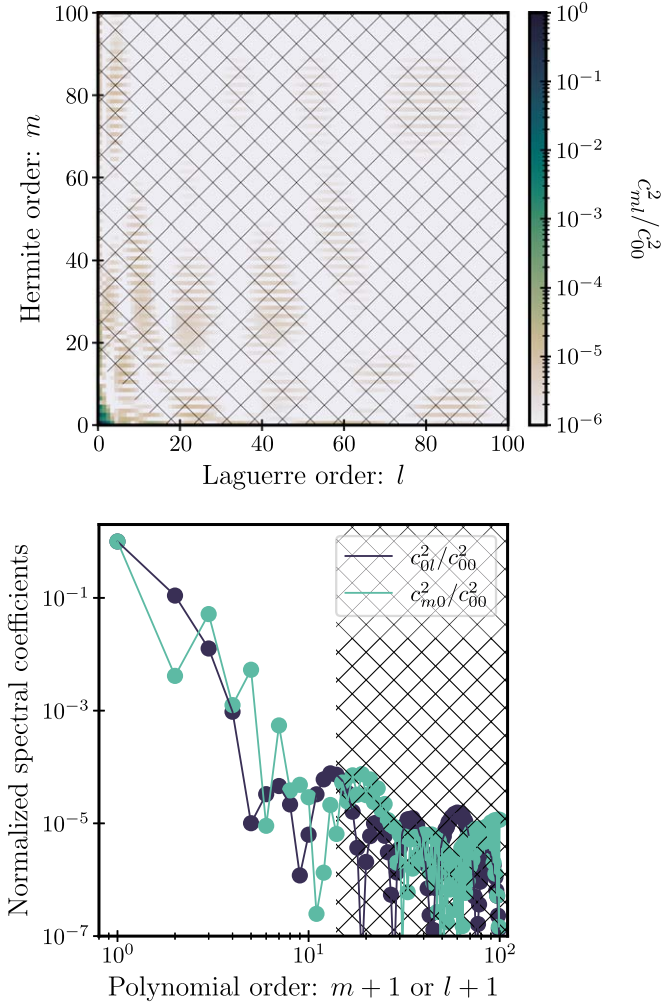
The inverse transform function is

$$F_{trunc}(v_\parallel, v_\perp) = \sum_{m,l=0}^{M,L} c_{ml}^{trunc} \, \psi_m(\hat{v}_\parallel) \, \Gamma_l^0(\hat{v}_\perp), \tag{17}$$

Table 1
The Moments (Equations (14a)) of the Background Electron VDF

n_e (cm^{-3})	$u_e^{\|}$ (km s^{-1})	$v_{th,e}^{\|}$ (km s^{-1})	$v_{th,e}^{\|}$ (km s^{-1})	$T_{\|}^e$ (eV)	$T_{\perp}^e$ (eV)	$q_{\|}^e$ (μW m^{-2})	$q_{\perp}^e$ (μW m^{-2})
27.3	418	2860	2560	23.3	18.6	49.2	12.6

Note. All calculations that require electron moments use these quantities.

Figure 2. Top panel: The squared Hermite–Laguerre spectral coefficients (Equation (16)) for the electron VDF. The color bar is normalized to c_{00}^2. The diagonal-hashed portion is set to zero for the inverse transform (Equation (18)). Bottom panel: Line plots of c_{0l}^2/c_{00}^2 (blue) and c_{m0}^2/c_{00}^2 (green). The spectral coefficients are large for small orders and decrease to $\sim 10^{-6}\, c_{00}^2$.

which follows from

$$c_{ml}^{\text{trunc}} = \begin{cases} c_{ml}, & \forall\ l \leqslant 14 - m, \\ 0, & \forall\ l > 14 - m. \end{cases} \tag{18}$$

Figure 2 shows the diagonal-hashed portion of spectral coefficients that are set to 0 with the definition of the truncated spectrum according to Equation (18). The bottom panel of Figure 1 displays the inverse transform function $F_{\text{trunc}}(v_{\|}, v_{\perp})$. After our noise reduction scheme by Hermite–Laguerre truncation, this function is a low-pass-filtered VDF on a grid in

$v_{\|}$, $v_{\perp}$, on which we compute the gradients in velocity space (see Appendix B).

Figure 3 shows a plot of the perpendicular and parallel slices of the VDFs that appear in Figure 1 (i.e., the magenta lines). The top panels compare the VDFs, where the interpolated VDF is clearly rougher, especially along the perpendicular velocity coordinate; moreover, the perpendicular slice is more rough. The middle panels are slices of the gradients along the direction of the slice. The gradient amplifies the structure in the two VDF representations, which is more severe for the perpendicular slice. The bottom panels compare the difference between the two methods to show that they are of order the one-particle noise level (i.e., a reasonable estimate for the noise of the instrument) and decrease with increasing speed.

3.5. Measurement of the Wave-frame Pitch-angle Gradient

We employ the Hermite–Laguerre expansion method to measure the wave-frame pitch-angle gradient (Equation (2)). The wave-frame pitch-angle gradient evaluated at the resonance is given by

$$\frac{\partial}{\partial \alpha} F_e(t, v_{\|}, v_{\perp}) \bigg|_{v_{\|}=V_e(k_{\|}^{\text{res}}, p)} = v_{\perp} \frac{\partial}{\partial v_{\|}} F_e(t, v_{\|}, v_{\perp}) \bigg|_{v_{\|}=V_e(k_{\|}^{\text{res}}, p)}$$
$$+ \frac{p\,\Omega_e}{k_{\|}^{\text{res}}} \frac{\partial}{\partial v_{\perp}} F_e(t, v_{\|}, v_{\perp}) \bigg|_{v_{\|}=V_e(k_{\|}^{\text{res}}, p)}, \tag{19}$$

where $k_{\|}^{\text{res}}$ is the unique parallel wavenumber participating in the resonant interaction at $v_{\|} = V_e(k_{\|}, p)$, according to Equation (8). The evaluation of $V_e(\boldsymbol{k}, p)$ requires knowledge of the dispersion relation to describe the observed whistler waves. Approximating the cold-plasma dispersion relation for parallel-propagating whistler waves ($\omega_{\text{whist}}(k_{\|})$) at frequencies $\omega_{\text{whist}} \gg \Omega_p$ leads to

$$k_{\|} = \frac{\omega_{\text{whist}}(k_{\|})}{c} \sqrt{1 - \frac{\omega_{p,e}^2/\omega_{\text{whist}}^2(k_{\|})}{1 - \Omega_e/\omega_{\text{whist}}(k_{\|})}}, \tag{20}$$

where $\omega_{p,e} = \sqrt{4\pi n_e q_e^2/m_e}$ is the electron plasma frequency.

To relate the wavenumber and frequency Fourier transforms, we use the expression $x_r = -V_{\text{SW}} t$, where x_r is a spatial coordinate along the solar wind direction, V_{SW} is the solar wind speed, and t is time. Then, using the plane wave assumption on the other two spatial dimensions, the magnetic field Fourier transform (Equation (6)) is

$$\tilde{\boldsymbol{B}}(k_{\|}) = \frac{2V_{\text{SW}}^3 T^2}{(2\pi)^3} \int_0^T dt\, \boldsymbol{B}(t, \boldsymbol{x})\, e^{-i2\pi f_{\text{sc}}(k_{\|})t}, \tag{21}$$
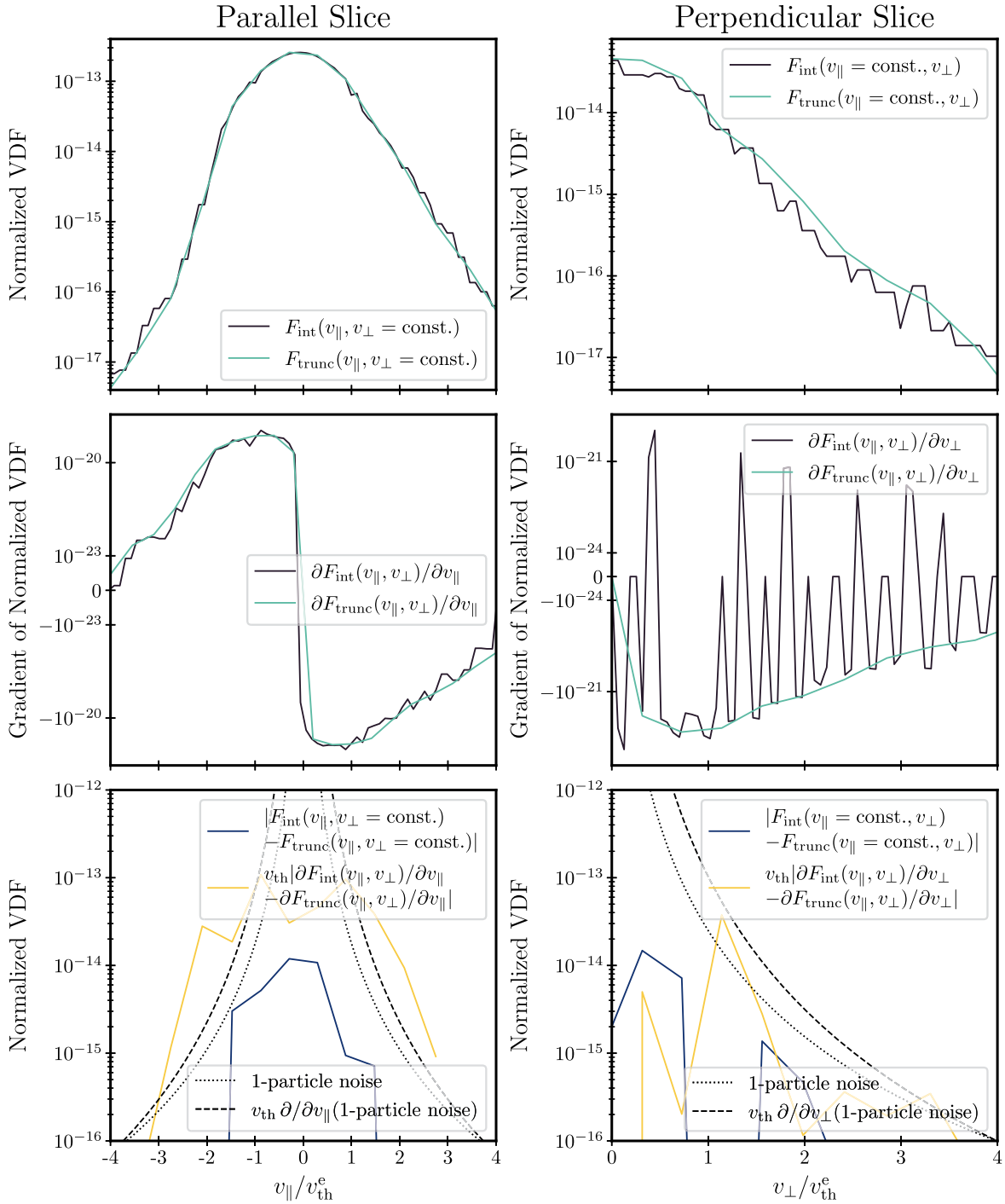
Figure 3. The left (right) column plots the normalized PSD along the horizontal (vertical) magenta lines in the middle and bottom panels of Figure 1 to visualize a parallel (perpendicular) slice of the VDF. The top panels compare the interpolated function in black (middle panel of Figure 1) and the Hermite–Laguerre method in green (bottom panel of Figure 1). The middle panels are the corresponding gradients. The bottom panels take the difference of the interpolated and Hermite–Laguerre method of both the VDF and the gradient of the VDF, and then compare them to the one-particle noise.

where T is the time duration of the measurement. The RPW instrument measures the magnetic field at frequency $f_{sc}(k_\parallel)$, where the subscript denotes the spacecraft frame. This defines the Doppler shift according to

$$2\pi f_{sc}(k_\parallel) = \omega_{whist}(k_\parallel) + k_\parallel |V_{SW}| \cos(\theta_{k,V_{SW}}), \qquad (22)$$

where we assume that the wave frequency $\omega(k)$ from Equation (4) is the whistler wave frequency ω_{whist}. The angle $\theta_{k,V_{SW}}$ is the angle between k and the solar wind direction, for which we make the observationally supported assumption that the whistler waves are quasi-parallel to the magnetic field. Inverting $f_{sc}(k_\parallel)$ for $k_\parallel(f_{sc})$ provides the wavenumber, which is valid in the narrowband enhancement in $f_{sc}(k_\parallel)$ that are identified to be whistler waves.

Figure 4 displays the order $p = -1$ wave-frame pitch-angle gradient (Equation (19)) of $F_{trunc}(v_\parallel, v_\perp)$ in the top left panel. Right-hand parallel waves do not resonate with electrons
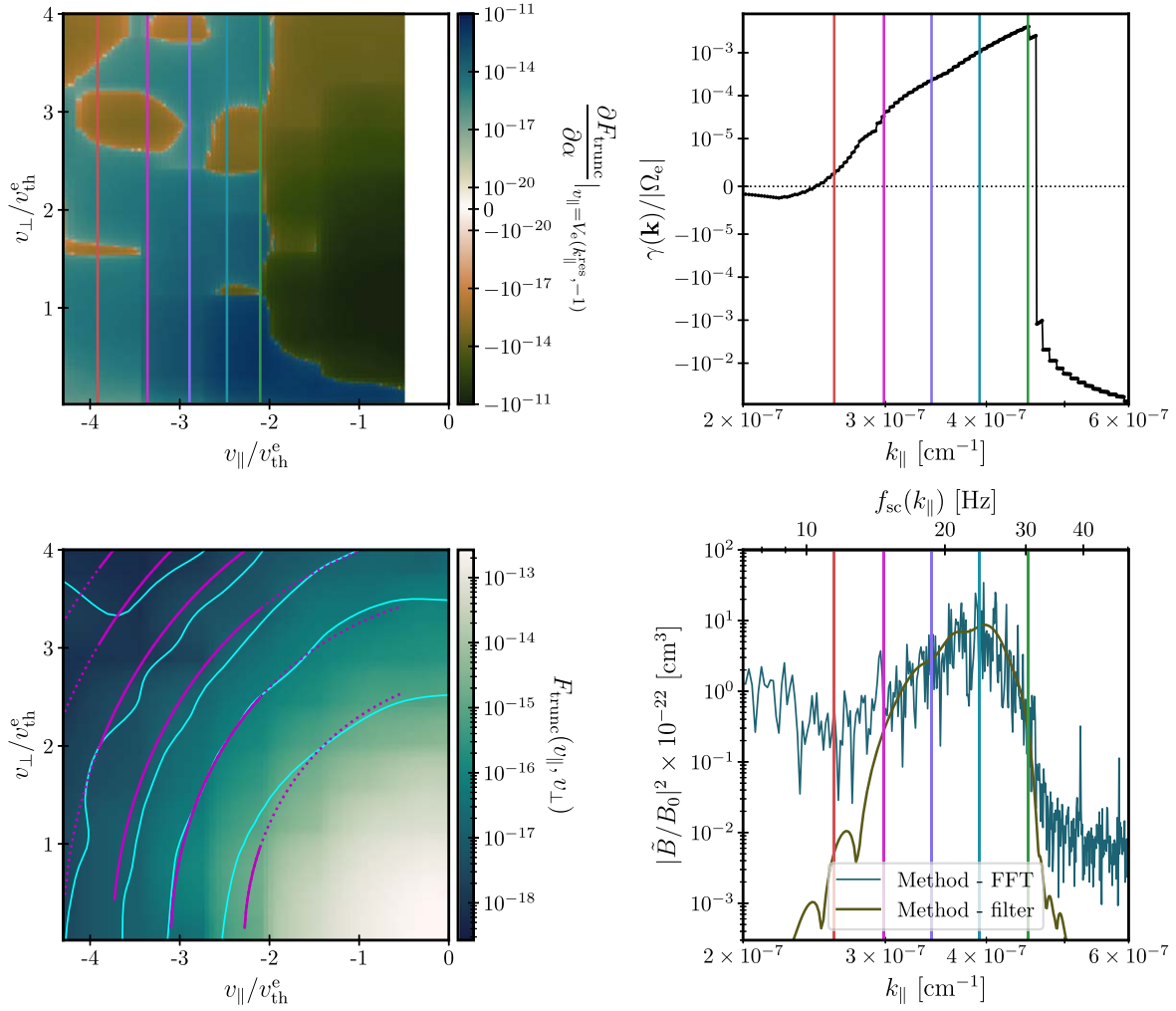
Figure 4. Top left: Equation (19) is mapped to a symmetric logarithmic scale. The colored lines map the velocity in the top left panel to/from the wavenumber of the right panels via the resonant velocity (Equation (8)) using the Doppler-shifted wavenumber (Equation (22)). Top right: growth rate (Equation (C12)). Bottom left: The low-pass-filtered VDF from Figure 1, accompanied by cyan contours at $[1.0 \times 10^{-18}, 4.0 \times 10^{-18}, 1.6 \times 10^{-17}, 6.3 \times 10^{-17}, 1.0 \times 10^{-15}]$ in units of the normalized VDF. The magenta lines follow from Equation (23). They are solid when the wavenumber maps to a positive growth rate, shown in the top right panel, and dotted when it maps to a damping rate. The bottom axis is the Doppler-shifted wavenumber (see discussion around Equation (22)). Bottom right: The measured magnetic field energy spectrum (Equation (3)) using a fast Fourier transform (blue) and using a set of filters (dark yellow). The upper axis shows the spacecraft frequency.

through the orders $p \neq -1$. The multicolored vertical lines map between the velocity (shown in the left panels of Figure 4) and wavenumber (right panels) by the resonant velocity (Equation (8)) using the analytical dispersion relation (Equation (20)) and the Doppler-shifted wavenumber (see Equation (22)). The overall direction of the diffusive flux in velocity space (indicated in the top left panel of Figure 4) in the region $v_\perp = [-3v_{th}^e, -2v_{th}^e]$, $v_\parallel = [0, 2v_{th}^e]$ moves to lower $v_\parallel$, $v_\perp$ to *fill in* the deficit region.

The top right panel of Figure 4 shows the growth rate, which we calculate in Appendix C, assuming the waves are right-handed parallel-propagating whistler waves. The growth rate, as the resonance function, is proportional to $\int dv_\perp v_\perp^2 \partial F_e / \partial \alpha$. The growth rate is positive in the region around the peak of the magnetic field enhancement (lower right panel) and maps to the deficit region of the electron VDF (shown in the left panels) via Equation (8).

The bottom left panel of Figure 4 is a magnified view of the deficit region of the electron VDF. The cyan lines are contours of F_{trunc}, and the magenta lines are contours of constant kinetic

energy in the wave frame,

$$v_\perp^2 + \left(\frac{\omega_{whist}(k_\parallel^{res})}{k_\parallel^{res}} - v_\parallel \right)^2 = \text{const.}, \quad (23)$$

where the velocity and wavenumber are evaluated at the resonance (Kennel 1966; Isenberg et al. 2001; Verscharen et al. 2022). The diffusion in velocity space (according to Equation (19)) is locally tangent to these contours. The magenta line is solid if the wavenumber maps to a resonant region, where the growth rate (shown in the top right panel) is positive ($\gamma(\mathbf{k}) > 0$), and otherwise the magenta line is dotted. If the contours of the VDF were everywhere tangent to these contours, the VDF would be marginally stable to the whistler wave. The cyan lines do not align with these contours, albeit similarly, therefore the VDF is close to marginal stability with respect to the whistler wave.

In the bottom right panel of Figure 4, we plot RPW's measurement of the normalized magnetic field energy
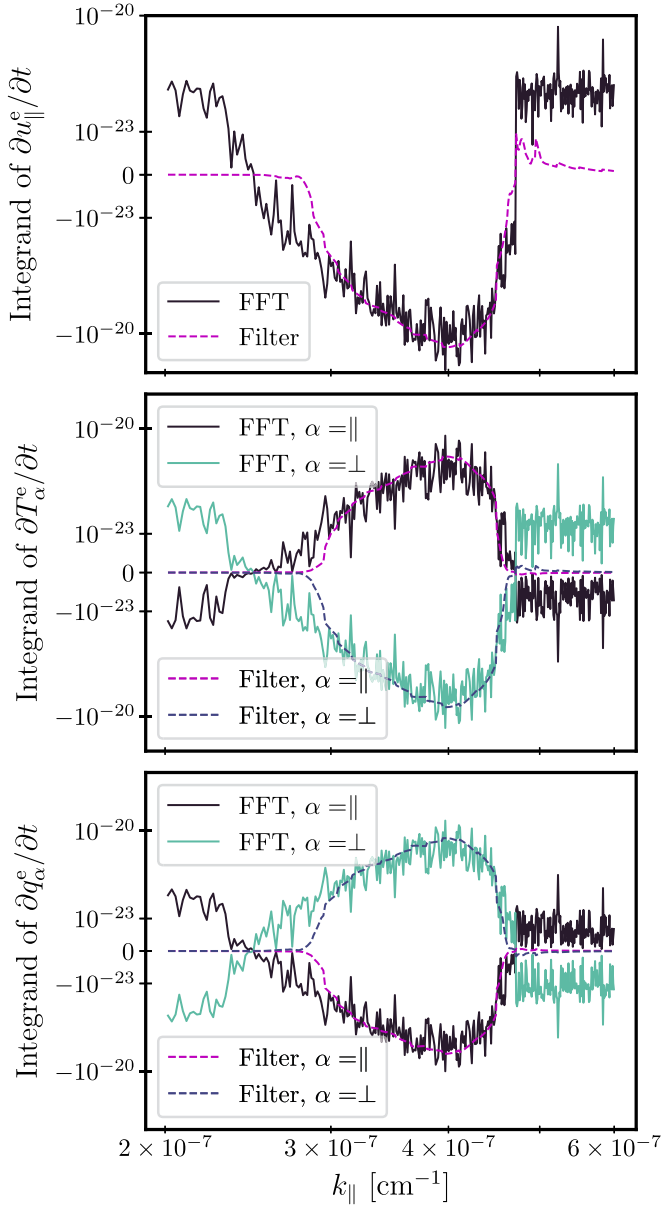
Figure 5. Top: the integrand of the parallel velocity in Equation (11). Middle: the integrand of the temperatures in Equation (11). Bottom: the integrand of the heat fluxes in Equation (11). The horizontal axes of these panels are the Doppler-shifted wavenumbers (see Equation (22)).

spectrum with two methods. The blue line is a Fast Fourier Transform (FFT), and the second method uses a set of filters. We apply a Butterworth filter, which captures the narrow band of whistler waves by setting the lower threshold to 15 Hz, the upper threshold to 33 Hz, and the cutoff order to 4 (i.e., the sharpness of the cutoff). The second filter is the Savitzky–Golay filter, which is a moving window (set to 30 points) that fits the data to a second-order polynomial to smooth the FFT. The filter method captures only the region consistent with whistler waves. The upper horizontal axis is the frequency in the spacecraft frame and the bottom axis is the Doppler-shifted wavenumber (see Equation (22)). The magnetic field enhancement occurs over a set of wavenumbers that is consistent with a positive growth rate (top right panel).

3.6. Measurement of the Rates of Change of the Moments

Figure 5 displays the integrand of the moments (Equation (11)), which constitutes the magnetic field energy spectrum and the wave-frame pitch-angle gradient (Equation (19)). Figure 5 shows the results based on both the filter and FFT energy spectrum methods (see bottom right panel of Figure 4). The filter method sets the integrands to zero outside of the resonant region, i.e., the span in wavenumber where the magnetic energy is unlikely to be generated by the instability.

According to Equation (11), the integral over wavevector of the quantities that appear in Figure 5 provides the rate of change of the moments. We present the results, for both the FFT and filtered method, in Table 2.

4. Discussion

4.1. Characterizing the Instability of the Electron VDF

The diffusion in phase space of the electron VDF leads to rates of change of the macroscopic moments, which are reported in Table 2. The decrease in $u_\parallel^e$ is consistent with conservation of momentum during quasi-parallel wave emission. The change in temperature indicates an increase in the anisotropy of the already anisotropic background VDF ($T_\perp^e / T_\parallel^e = 0.80$). In the deficit region, the diffusive flux of particles in velocity space alters both $q_\parallel^e$ and $q_\perp^e$ as defined in Equations (14e) and (14f). This process decreases $q_\parallel^e$ and increases $q_\perp^e$.

Table 2 reports the rates of change of the moments. To obtain the total change in the moments, integration of the rates (which are a function of time) over the total relaxation time (or the quasilinear diffusion time) is required. Tong et al. (2019a) study the quasilinear diffusion time estimate of Karpman (1974) and find a large range of values, from a few thousand seconds to just a few seconds, inversely correlated with β_e. Using their calculation, we confirm that the quasilinear approach is applicable (see discussions by Tong et al. 2019a and Berčič et al. 2021b), and calculate a quasilinear diffusion time of 0.25 s. While this is longer than the resolution of SWA/EAS's novel burst mode of 0.125 s (Owen et al. 2021), so in principle a diffusion time of this scale is measurable, this timescale is questionably small. For example, the observation might be near to marginal stability, so this estimate is not the true quasilinear diffusion time. The instability saturation, its quasilinear diffusion time, the variation of the rates during the regulation process, etc., for realistic solar wind conditions, would be worthwhile to investigate. For example, it is not generally known what regulation mechanisms are slow/fast enough to be measured by spacecraft.

4.2. The Hermite–Laguerre Polynomials

Spectral techniques have been used in plasma physics in the context of simulations (Delzanno 2015; Parker & Dellar 2015; Camporeale et al. 2016; Loureiro et al. 2016; Mandell et al. 2018; Koshkarov et al. 2021), linear Vlasov–Maxwell solutions (Grant 1967; Camporeale et al. 2006), transport theory (Grad 1949; Hunana et al. 2022), and for weakly collisional plasmas (Schekochihin et al. 2016; Servidio et al. 2017; Pezzi et al. 2019a, 2019b). Spectral techniques have also been used in the context of observational analysis (Dum et al. 1980; Viñas & Gurgiolo 2009; Servidio et al. 2017; Bowen et al. 2022).

Table 2
The Results of Integrating Equation (11)

Method	$\partial u_{\mathrm{e}}^{\parallel}/\partial t$ (km s^{-2})	$\partial T_{\parallel}^{\mathrm{e}}/\partial t$ (eV s^{-1})	$\partial T_{\perp}^{\mathrm{e}}/\partial t$ (eV s^{-1})	$\partial q_{\parallel}^{\mathrm{e}}/\partial t$ (μW m^{-2} s^{-1})	$\partial q_{\perp}^{\mathrm{e}}/\partial t$ (μW m^{-2} s^{-1})
FFT	−1.24	0.0949	−0.313	−0.155	0.341
Filtered	−1.22	0.0936	−0.309	−0.150	0.330

The choice of the Hermite–Laguerre polynomials has been questioned in the past (see Dum et al. 1980), due to the fact that spectral coefficients converge slowly and the thermal speed is time and space dependent (see Appendix of Camporeale et al. 2006 for the latter issue). Here, we discuss the issue of convergence when using Legendre polynomials, as done by Dum et al. (1980), considering the pitch angle as the argument. Because electromagnetic microinstabilities alter the pitch angle in the wave frame (translation in $v_{\parallel}$), it is necessary that the derivative orthogonal to the plasma-frame pitch angle be evaluated, and therefore an additional variable must be introduced. While this is possible, there is no obvious two-dimensional Maxwellian-like basis function that retains the orthonormal properties with the plasma-frame pitch angle.

However, as we show with our study, the Hermite–Laguerre expansion provides a method to determine the trustworthy VDF grid resolution, and thus a trustworthy VDF, from in situ VDF measurements by truncating the spectral coefficients at the noise floor (see Section 3.4). Underresolving the VDF with either insufficient VDF resolution or low-order truncation of the spectral series results in (very) poor results: wave damping and consequently a change in sign of all the rates. Over-resolving the VDF through very high resolution of the velocity space or retaining spectral coefficients in the presumed noise floor provides similar results, because the noise tends to cancel when computing the velocity space integrals (see Equation (11)).

5. Conclusions

In this work, we study Solar Orbiter observations of deficit-generated whistler waves. We present direct evidence of the regulation of the electron VDF, in particular the parallel heat flux, by microinstabilities. The analysis confirms that the unstable region of the electron VDF during our observed interval is the deficit region. Thus, by quasilinear diffusion, the deficit is being *filled in*, decreasing the parallel electron heat flux. The primary measurement is the wave-frame pitch-angle gradient of the electron VDF, shown in the top panel of Figure 4. We present the measurement of the rates of change of the moments in Figure 5 and record the results in Table 2.

The key piece of data analysis is shown in Section 3.4, where the implementation of the Hermite–Laguerre expansion as a velocity-space low-pass filter provides a trustworthy VDF. The technique is well-suited to measure the wave-frame pitch-angle gradient because, first, the VDF is smoother without noise, and the Hermite–Laguerre polynomials follow recursion relations for gradients and products.

Our method (i.e., Hermite–Laguerre expansion) cleans spurious signals in the particle VDFs and retains only trustworthy features in the electron VDF. More broadly, the electromagnetic and collisional terms in the Boltzmann equation are proportional to the velocity space gradient of the VDF, so our analysis technique is widely applicable to measuring kinetic plasma physics processes.

Model VDFs (e.g., drifting bi-Maxwellians) reduce the complexity of numerical evaluations of the growth and effects of microinstabilities and act to classify them so they can be compared. However, this work highlights the need for more detailed knowledge of the VDF in order to reliably evaluate the behavior of microinstabilities and the subsequent quasilinear evolution in collisionless plasmas (see Astfalk & Jenko 2017; Dorfman et al. 2017; Astfalk & Jenko 2018; Verscharen et al. 2018).

The generation mechanism for whistler waves during this interval is the deficit in the electron VDF, which is ultimately connected to the large-scale ambipolar electric field. Studies of whistler waves in the solar wind suggest wave generation apparently through local solar wind structures (i.e., stream interactions, electron deficit, and magnetic field inhomogeneities), but our current understanding of linear theory does not properly predict whistler wave occurrence (Lacombe et al. 2014; Tong et al. 2019b; Jagarlamudi et al. 2020; Berčič et al. 2021b; Jagarlamudi et al. 2021; Karbashewski et al. 2023). This work highlights the need for a better understanding of wave generation mechanisms both in theory and observations in order to better inform models of the solar wind (Horaites et al. 2017; Boldyrev & Horaites 2019; Shaaban et al. 2019; Yoon et al. 2019; Schroeder et al. 2021; Jeong et al. 2022).

The deficit makes a significant contribution to the heat flux in the near-Sun solar wind (Halekas et al. 2020), and further work is necessary to model wave–particle interactions as a regulation mechanism on the illusive electron heat flux. Future work will use the analysis technique we present to address the multitude of relevant instabilities through detailed analyses of the VDF.

Appendix A
Derivation of General Moment Theory

We multiply Equation (1) by a general term $\mathcal{G}(t, \boldsymbol{x}, \boldsymbol{v})$, to act as the integrand of the moment, where the requirement on $\mathcal{G}(t, \boldsymbol{x}, \boldsymbol{v})$ is that the total integral is zero when integrated over the full velocity space. The integral in the cylindrical coordinate system gives

$$
2\pi \int_{-\infty}^{\infty} dv_{\parallel} \int_{0}^{\infty} dv_{\perp} \, v_{\perp} \mathcal{G}(t, \boldsymbol{x}, \boldsymbol{v}) \frac{\partial}{\partial t} F_s(t, v_{\parallel}, v_{\perp})
$$
$$
= \frac{1}{(2\pi)^3} \int_{-\infty}^{\infty} d^3k \, \hat{\mathcal{B}}(\boldsymbol{k}) \, 2\pi \int_{-\infty}^{\infty} dv_{\parallel}
$$
$$
\times \int_{0}^{\infty} dv_{\perp} \, \mathcal{G}(t, \boldsymbol{x}, \boldsymbol{v}) \frac{\partial}{\partial \alpha} v_{\perp} \nu_s(\boldsymbol{k}, v_{\parallel}, v_{\perp}) \frac{\partial}{\partial \alpha} F_s(t, v_{\parallel}, v_{\perp}), \quad \text{(A1)}
$$

where we assume gyrotropy of the VDF. Product rule on the first wave-frame pitch-angle gradient gives

$$
2\pi \int_{-\infty}^{\infty} dv_{\parallel} \int_{0}^{\infty} dv_{\perp} \, v_{\perp} \mathcal{G}(t, \boldsymbol{x}, \boldsymbol{v}) \frac{\partial}{\partial t} F_s(t, v_{\parallel}, v_{\perp})
$$
$$
= \frac{1}{(2\pi)^3} \int_{-\infty}^{\infty} d^3k \, \hat{\mathcal{B}}(\boldsymbol{k}) \, 2\pi \int_{-\infty}^{\infty} dv_{\parallel} \int_{0}^{\infty} dv_{\perp}
$$
$$
\times \left[\frac{\partial}{\partial \alpha} \mathcal{G}(t, \boldsymbol{x}, \boldsymbol{v}) v_{\perp} \nu_s(\boldsymbol{k}, v_{\parallel}, v_{\perp}) \frac{\partial}{\partial \alpha} F_s(t, v_{\parallel}, v_{\perp}) \right.
$$
$$
\left. - \left(\frac{\partial}{\partial \alpha} \mathcal{G}(t, \boldsymbol{x}, \boldsymbol{v}) \right) v_{\perp} \nu_s(\boldsymbol{k}, v_{\parallel}, v_{\perp}) \frac{\partial}{\partial \alpha} F_s(t, v_{\parallel}, v_{\perp}) \right]. \quad \text{(A2)}
$$

The first term in the large square brackets integrates to zero considering $F_s(t, v_{\parallel}, v_{\perp})$ approaches zero faster than the rest of the integrand. The second term resolves due to the δ function in ν_s (Equation (7)) requiring $v_{\parallel} = V_s(\boldsymbol{k}, p)$. The left-hand side of Equation (A2) is rearranged with the product rule to give

$$
2\pi \frac{\partial}{\partial t} \int_{-\infty}^{\infty} dv_{\parallel} \int_{0}^{\infty} dv_{\perp} \, v_{\perp} \mathcal{G}(t, \boldsymbol{x}, \boldsymbol{v}) F_s(t, v_{\parallel}, v_{\perp})
$$
$$
= \frac{\Omega_s^2}{4\pi} \int_{-\infty}^{\infty} d^3k \, \hat{\mathcal{B}}(\boldsymbol{k}) \frac{1}{k_{\parallel}} \sum_{p=-\infty}^{\infty}
$$
$$
\times \int_{0}^{\infty} dv_{\perp} \, \mathcal{R}_s(\boldsymbol{k}, v_{\perp}, p) \frac{1}{v_{\perp}} \frac{\partial}{\partial \alpha} \mathcal{G}(t, \boldsymbol{x}, \boldsymbol{v}) \bigg|_{v_{\parallel} = V_s(\boldsymbol{k}, p)}
$$
$$
+ 2\pi \int_{-\infty}^{\infty} dv_{\parallel} \int_{0}^{\infty} dv_{\perp} \, v_{\perp} F_s(t, v_{\parallel}, v_{\perp}) \frac{\partial}{\partial t} \mathcal{G}(t, \boldsymbol{x}, \boldsymbol{v}), \quad \text{(A3)}
$$

where

$$
\mathcal{R}_s(\boldsymbol{k}, v_{\perp}, p) = 2\pi^2 \frac{k_{\parallel}}{|k_{\parallel}|} \left| \frac{v_{\perp}}{2} \left[J_{p-1}\left(\frac{k_{\perp} v_{\perp}}{\Omega_s} \right) e^+ \right. \right.
$$
$$
+ J_{p+1}\left(\frac{k_{\perp} v_{\perp}}{\Omega_s} \right) e^- \right]
$$
$$
\left. + V_s(k, p) J_p\left(\frac{k_{\perp} v_{\perp}}{\Omega_s} \right) e^z \right|^2 \left(-\frac{\partial}{\partial \alpha} F_s(t, v_{\parallel}, v_{\perp})_{v_{\parallel} = V_s(k, p)} \right).
$$
$$
\text{(A4)}
$$

Equation (A3) describes the rate of change of the moment corresponding to $\mathcal{G}(t, \boldsymbol{x}, \boldsymbol{v})$. The result written here is a modified version of Equation (26) of Marsch & Tu (2001), because the $v_{\perp}$ integral is modified by the presence of higher-order polynomials in $v_{\perp}$, such that their definition does not generalize to higher-order moments.

Appendix B
Hermite–Laguerre Polynomials

The Hermite functions are

$$
\psi_m(x) = \frac{1}{(2^m m! \sqrt{\pi})^{1/2}} e^{-x^2/2} H_m(x), \quad \text{(B1)}
$$

where the Hermite polynomials are

$$
H_m(x) = (-1)^m e^{x^2} \frac{d^m}{dx^m} e^{-x^2}, \quad \text{(B2)}
$$

and the orthonormal condition is

$$
\int_{-\infty}^{\infty} dx \, \psi_m(x) \psi_n(x) = \delta_{mn}. \quad \text{(B3)}
$$

The recursion relations for the Hermite functions are

$$
\frac{\partial}{\partial x} \psi_m(x) = \sqrt{\frac{m}{2}} \psi_{m-1}(x) - \sqrt{\frac{m+1}{2}} \psi_{m+1}(x), \quad \text{(B4)}
$$

$$
x \, \psi_m(x) = \sqrt{\frac{m}{2}} \psi_{m-1}(x) + \sqrt{\frac{m+1}{2}} \psi_{m+1}(x). \quad \text{(B5)}
$$

The associated Laguerre functions, polynomials, and the orthonormal condition are

$$
\Gamma_n^k(x) = \sqrt{\frac{n!}{(n+k)!}} e^{-x/2} x^{k/2} L_n^k(x), \quad \text{(B6)}
$$

$$
L_n^k(x) = \frac{e^x x^{-k}}{n!} \frac{d^n}{dx^n} (e^{-x} x^{n+k}), \quad \text{(B7)}
$$

$$
\int_{0}^{\infty} dx \, \Gamma_n^k(x) \Gamma_m^k(x) = \delta_{nm}. \quad \text{(B8)}
$$

The recursion relations for the associated Laguerre polynomials are

$$
\frac{\partial}{\partial x} L_n^k(x) = -L_{n-1}^{k+1}(x), \quad \text{(B9)}
$$

and

$$
x L_n^k(x) = (n+k) L_n^{k-1}(x) - (n+1) L_{n+1}^{k-1}(x). \quad \text{(B10)}
$$

Therefore, the associated Laguerre functions follow the relations

$$\frac{\partial}{\partial x}\Gamma_n^k(x) = \Gamma_n^k(x)\left(\frac{k}{2x} - \frac{1}{2}\right) - \sqrt{\frac{n}{x}}\,\Gamma_{n-1}^{k+1}(x), \quad \text{(B11)}$$

$$x\,L_n^k(x) = (n+k)L_n^{k-1}(x) - (n+1)L_{n+1}^{k-1}(x). \quad \text{(B12)}$$

The choice of these functions becomes clear when considering the basis function

$$\psi_0(x)\,\Gamma_0^0(y) = \pi^{-1/4}\,e^{-x^2/2}\,e^{-y/2}, \quad \text{(B13)}$$

so that, if $x = \sqrt{2}\,v_\parallel/v_{\mathrm{th}}^\parallel$ and $y = 2(v_\perp/v_{\mathrm{th}}^\perp)^2$,

$$\psi_0\!\left(\frac{v_\parallel}{v_{\mathrm{th}}^\parallel}\right)\Gamma_0^0\!\left(\left(\frac{v_\perp}{v_{\mathrm{th}}^\perp}\right)^2\right) = \pi^{-1/4}\exp\!\left[-\left(\frac{v_\parallel}{v_{\mathrm{th}}^\parallel}\right)^2 - \left(\frac{v_\perp}{v_{\mathrm{th}}^\perp}\right)^2\right], \quad \text{(B14)}$$

which is the unnormalized bi-Maxwellian in two-dimensional Cartesian coordinates.

Appendix C
The Growth Rate for Parallel Whistler Waves

Following Kennel & Wong (1967), in our notation, the growth is approximately

$$\frac{\gamma(\mathbf{k})}{\omega(\mathbf{k})} = \frac{k_\parallel}{|k_\parallel|}\sum_s \sum_{p=-\infty}^{\infty}\left(\frac{\omega_{\mathrm{p},s}^2}{\omega(\mathbf{k})^2}\right)$$

$$\times\,\frac{\pi}{16}\int_0^\infty dv_\perp \int_{-\infty}^\infty dv_\parallel v_\perp^2\,\delta(v_\parallel - V_s(\mathbf{k},p))\frac{1}{W(\omega,\mathbf{k})}$$

$$\times\,\left|\,J_{p-1}\!\left(\frac{k_\perp v_\perp}{\Omega_s}\right)E^+(\mathbf{k}) + J_{p+1}\!\left(\frac{k_\perp v_\perp}{\Omega_s}\right)E^-(\mathbf{k})\right.$$

$$\left. +\,\frac{v_\parallel}{v_\perp}J_p\!\left(\frac{k_\perp v_\perp}{\Omega_s}\right)E_z(\mathbf{k})\,\right|^2\,\frac{\partial}{\partial\alpha}F_s(v_\perp, v_\parallel), \quad \text{(C1)}$$

where

$$W(\omega,\mathbf{k}) = \frac{1}{16\pi}\left[\tilde{\mathbf{B}}^*(\mathbf{k})\cdot\tilde{\mathbf{B}}(\mathbf{k}) + \tilde{\mathbf{E}}^*(\mathbf{k})\cdot\left(\frac{\partial}{\partial\omega}\omega\epsilon^{\mathrm{H}}(\omega,\mathbf{k})\right)\cdot\tilde{\mathbf{E}}(\mathbf{k})\right] \quad \text{(C2)}$$

is the wave energy and $\epsilon^{\mathrm{H}}(\omega,\mathbf{k}) = (\epsilon^\dagger(\omega,\mathbf{k}) + \epsilon(\omega,\mathbf{k}))/2$ is the Hermitian part of the dielectric tensor $\epsilon(\omega,\mathbf{k})$, and the superscript $\dagger$ denotes the conjugate transpose. The Fourier amplitudes of the electric field are

$$E^+(\mathbf{k}) = \frac{1}{\sqrt{2}}(\tilde{E}_x(\mathbf{k}) - i\tilde{E}_y(\mathbf{k})) \quad \text{(C3)}$$

and

$$E^-(\mathbf{k}) = \frac{1}{\sqrt{2}}(\tilde{E}_x(\mathbf{k}) + i\tilde{E}_y(\mathbf{k})), \quad \text{(C4)}$$

where the Fourier amplitudes of the electric field are related to the Fourier amplitudes of the magnetic field by Faraday's law,

$$\tilde{\mathbf{B}}(\mathbf{k}) = \frac{c}{\tilde{\omega}(\mathbf{k})}\mathbf{k}\times\tilde{\mathbf{E}}(\mathbf{k}). \quad \text{(C5)}$$

For the dielectric tensor and consequently the dispersion relation, we use the cold-plasma dielectric tensor. Following Stix (1992),

$$\epsilon\cdot\mathbf{E} = \begin{pmatrix} S & -iD & 0 \\ iD & S & 0 \\ 0 & 0 & P \end{pmatrix}\begin{pmatrix} E_x \\ E_y \\ E_z \end{pmatrix}, \quad \text{(C6)}$$

where

$$S = \frac{1}{2}(R+L), \qquad D = \frac{1}{2}(R-L),$$

$$R = 1 - \sum_s \frac{\omega_{\mathrm{p},s}^2}{\omega(\omega + \Omega_s)}, \qquad L = 1 - \sum_s \frac{\omega_{\mathrm{p},s}^2}{\omega(\omega - \Omega_s)}$$

$$P = 1 - \sum_s \frac{\omega_{\mathrm{p},s}^2}{\omega^2}. \quad \text{(C7)}$$

For parallel-propagating electromagnetic waves with $\mathbf{k} = k_\parallel\hat{\mathbf{b}}$, we find $L = R = \mathbf{k}^2 c^2/\omega(\mathbf{k})^2$, and for $P = 0$. Using $\Omega_{\mathrm{p}} \ll \omega(\mathbf{k}) \ll |\Omega_{\mathrm{e}}|$ for the whistler wave, we find

$$\tilde{\omega}(\mathbf{k}) = |\Omega_{\mathrm{e}}|d_{\mathrm{e}}^2 k_\parallel^2,$$

$$\epsilon^{\mathrm{H}} = \epsilon = \begin{pmatrix} \mathbf{k}^2 c^2/\omega(\mathbf{k})^2 & 0 & 0 \\ 0 & \mathbf{k}^2 c^2/\omega(\mathbf{k})^2 & 0 \\ 0 & 0 & 0 \end{pmatrix}. \quad \text{(C8)}$$

Next, using the fact they these are right-handed circular waves, we find that the wave energy $W(\omega,\mathbf{k})$ and normalized wave energy $\hat{W}(\omega,\mathbf{k})$ are

$$W(\omega,\mathbf{k}) = \frac{1}{16\pi}[\hat{B}_x(\mathbf{k})^2 + \hat{B}_y(\mathbf{k})^2]$$

$$\times\left[1 + \left(\frac{\omega(\mathbf{k})}{c\,k_\parallel}\right)^2\left(1 - \frac{\omega_{\mathrm{p,p}}^2}{A^2} - \frac{\omega_{\mathrm{p,e}}^2}{A\,B}\right)\left(1 + \frac{\omega_{\mathrm{p,p}}^2}{A^2} + \frac{\omega_{\mathrm{p,e}}^2}{B^2}\right)\right]$$

$$\hat{W}(\omega,\mathbf{k}) = \frac{1}{16\pi}\left(\frac{c\,k_\parallel}{\omega(\mathbf{k})}\right)^2$$

$$\times\left[1 + \left(\frac{\omega(\mathbf{k})}{c\,k_\parallel}\right)^2\left(1 - \frac{\omega_{\mathrm{p,p}}^2}{A^2} - \frac{\omega_{\mathrm{p,e}}^2}{A\,B}\right)\left(1 + \frac{\omega_{\mathrm{p,p}}^2}{A^2} + \frac{\omega_{\mathrm{p,e}}^2}{B^2}\right)\right], \quad \text{(C9)}$$

where

$$A = |\Omega_{\mathrm{e}}|d_{\mathrm{e}}^2 k_\parallel^2 - |\Omega_{\mathrm{e}}|, \quad \text{(C10)}$$

and

$$B = |\Omega_{\mathrm{e}}|d_{\mathrm{e}}^2 k_\parallel^2. \quad \text{(C11)}$$

With these results, Equation (C1) yields

$$\gamma(\mathbf{k}) = \left(\frac{k_\parallel}{|k_\parallel|}\right)\left(\frac{\omega_{\mathrm{p,e}}^2}{\omega^2}\right)\frac{\omega(\mathbf{k})}{2\hat{W}(\omega,\mathbf{k})}\frac{\pi}{16}$$

$$\times\left.\int_0^\infty dv_\perp v_\perp^2\frac{\partial}{\partial\alpha}F_{\mathrm{e}}(v_\perp, v_\parallel)\right|_{v_\parallel = V_{\mathrm{e}}(\mathbf{k},p)}. \quad \text{(C12)}$$

ORCID iDs

Jesse T. Coburn ⓘ https://orcid.org/0000-0002-2576-0992
Daniel Verscharen ⓘ https://orcid.org/0000-0002-0497-1096
Christopher J. Owen ⓘ https://orcid.org/0000-0002-5982-4667

Milan Maksimovic ⓘ https://orcid.org/0000-0001-6172-5062
Timothy S. Horbury ⓘ https://orcid.org/0000-0002-7572-4690
Christopher H. K. Chen ⓘ https://orcid.org/0000-0003-4529-3620
Fan Guo ⓘ https://orcid.org/0000-0003-4315-3755
Xiangrong Fu ⓘ https://orcid.org/0000-0002-4305-6624
Jingting Liu ⓘ https://orcid.org/0009-0003-9856-5949
Joel B. Abraham ⓘ https://orcid.org/0000-0002-6305-3252
Georgios Nicolaou ⓘ https://orcid.org/0000-0003-3623-4928
Maria Elena Innocenti ⓘ https://orcid.org/0000-0002-5782-0013
Alfredo Micera ⓘ https://orcid.org/0000-0001-9293-174X
Vamsee Krishna Jagarlamudi ⓘ https://orcid.org/0000-0001-6287-6479

References

Abraham, J. B., Verscharen, D., Wicks, R. T., et al. 2022, ApJ, 941, 145
Astfalk, P., & Jenko, F. 2017, JGRA, 122, 89
Astfalk, P., & Jenko, F. 2018, JGRA, 123, 7153
Bale, S. D., Pulupa, M., Salem, C., Chen, C. H. K., & Quataert, E. 2013, ApJL, 769, L22
Berčič, L., Larson, D., Whittlesey, P., et al. 2020, ApJ, 892, 88
Berčič, L., Maksimović, M., Halekas, J. S., et al. 2021a, ApJ, 921, 83
Berčič, L., Verscharen, D., Owen, C. J., et al. 2021b, A&A, 656, A31
Boldyrev, S., & Horaites, K. 2019, MNRAS, 489, 3412
Bowen, T. A., Chandran, B. D. G., Squire, J., et al. 2022, PhRvL, 129, 165101
Camporeale, E., Delzanno, G., Bergen, B., & Moulton, J. 2016, CoPhC, 198, 47
Camporeale, E., Delzanno, G. L., Lapenta, G., & Daughton, W. 2006, PhPl, 13, 092110
Delzanno, G. 2015, JCoPh, 301, 338
Dorfman, S., Hietala, H., Astfalk, P., & Angelopoulos, V. 2017, GeoRL, 44, 2120
Dum, C. T., Marsch, E., & Pilipp, W. 1980, JPlPh, 23, 91
Feldman, W. C., Asbridge, J. R., Bame, S. J., Montgomery, M. D., & Gary, S. P. 1975, JGR, 80, 4181
Gary, S. P. 1993, Theory of Space Plasma Microinstabilities (Cambridge, UK: Cambridge Univ. Press)
Gary, S. P., Feldman, W. C., Forslund, D. W., & Montgomery, M. D. 1975, JGR, 80, 4197
Gary, S. P., Scime, E. E., Phillips, J. L., & Feldman, W. C. 1994, JGRA, 99, 23391
Gary, S. P., Skoug, R. M., & Daughton, W. 1999, PhPl, 6, 2607
Grad, H. 1949, Comm. Pure Appl. Math., 2, 331
Grant, F. C. 1967, PhFl, 10, 696
Halekas, J. S., Bale, S. D., Berthomier, M., et al. 2023, ApJ, 952, 26
Halekas, J. S., Whittlesey, P., Larson, D. E., et al. 2020, ApJS, 246, 22
Hollweg, J. V. 1974, JGR, 79, 3845
Horaites, K., Boldyrev, S., Wilson, L. B., Viñas, A. F., & Merka, J. 2018, MNRAS, 474, 115
Horbury, T. S., O'Brien, H., Blazquez, I. C., et al. 2020, A&A, 642, A9
Hunana, P., Passot, T., Khomenko, E., et al. 2022, ApJS, 260, 26
Isenberg, P. A., Lee, M. A., & Hollweg, J. V. 2001, JGRA, 106, 5649

Jagarlamudi, V. K., Alexandrova, O., Berčič, L., et al. 2020, ApJ, 897, 118
Jagarlamudi, V. K., Wit, T. D. d., Froment, C., et al. 2021, A&A, 650, A9
Jeong, S. Y., Verscharen, D., Vocks, C., et al. 2022, ApJ, 927, 162
Jockers, K. 1970, A&A, 6, 219
Karbashewski, S., Agapitov, O. V., Kim, H. Y., et al. 2023, ApJ, 947, 73
Karpman, V. I. 1974, SSRv, 16, 361
Kennel, C. F. 1966, PhFl, 9, 2377
Kennel, C. F., & Wong, H. V. 1967, JPlPh, 1, 75
Koshkarov, O., Manzini, G., Delzanno, G., Pagliantini, C., & Roytershteyn, V. 2021, CoPhC, 264, 107866
Lacombe, C., Alexandrova, O., Matteini, L., et al. 2014, ApJ, 796, 5
Landi, S., Matteini, L., & Pantellini, F. 2012, ApJ, 760, 143
Landi, S., & Pantellini, F. 2003, A&A, 400, 769
Lazar, M., Pierrard, V., Shaaban, S. M., Fichtner, H., & Poedts, S. 2017, A&A, 602, A44
Lazar, M., Shaaban, S. M., Fichtner, H., & Poedts, S. 2018, PhPl, 25, 022902
Loureiro, N., Dorland, W., Fazendeiro, L., et al. 2016, CoPhC, 206, 45
Maksimovic, M., Bale, S. D., Chust, T., et al. 2020, A&A, 642, A12
Maksimovic, M., Pierrard, V., & Lemaire, J. F. 1997, A&A, 324, 725
Mandell, N. R., Dorland, W., & Landreman, M. 2018, JPlPh, 84, 905840108
Marsch, E. 2006, LRSP, 3, 1
Marsch, E., & Tu, C. 2001, JGRA, 106, 227
Micera, A., Zhukov, A. N., López, R. A., et al. 2021, ApJ, 919, 42
Müller, D., Cyr, O. C. S., Zouganelis, I., et al. 2020, A&A, 642, A1
Owen, C. J., Abraham, J. B., Nicolaou, G., et al. 2022, Univ, 8, 509
Owen, C. J., Bruno, R., Livi, S., et al. 2020, A&A, 642, A16
Owen, C. J., Kataria, D. O., Berčič, L., et al. 2021, A&A, 656, L9
Parker, J. T., & Dellar, P. J. 2015, JPlPh, 81, 305810203
Pezzi, O., Perrone, D., Servidio, S., et al. 2019a, ApJ, 887, 208
Pezzi, O., Valentini, F., Servidio, S., Camporeale, E., & Veltri, P. 2019b, PPCF, 61, 054005
Pierrard, V., & Lemaire, J. 1996, JGRA, 101, 7923
Salem, C., Hubert, D., Lacombe, C., et al. 2003, ApJ, 585, 1147
Salem, C. S., Pulupa, M., Bale, S. D., & Verscharen, D. 2023, A&A, 675, A162
Schekochihin, A. A., Parker, J. T., Highcock, E. G., et al. 2016, JPlPh, 82, 905820212
Schroeder, J. M., Boldyrev, S., & Astfalk, P. 2021, MNRAS, 507, 1329
Scime, E. E., Bame, S. J., Feldman, W. C., et al. 1994, JGRA, 99, 23401
Scudder, J. D. 1992, ApJ, 398, 299
Scudder, J. D. 2019, ApJ, 885, 138
Servidio, S., Chasapis, A., Matthaeus, W. H., et al. 2017, PhRvL, 119, 205101
Shaaban, S. M., Lazar, M., Yoon, P. H., & Poedts, S. 2019, A&A, 627, A76
Shapiro, V., & Shevchenko, V. 1964, Sov. Phys. JETP, 18, 1109
Stix, T. H. 1992, Waves in Plasmas (Melville, NY: American Institute of Physics)
Štvěrák, v., Trávníček, P. M., & Hellinger, P. 2015, JGRA, 120, 8177
Tong, Y., Vasko, I. Y., Artemyev, A. V., Bale, S. D., & Mozer, F. S. 2019a, ApJ, 878, 41
Tong, Y., Vasko, I. Y., Pulupa, M., et al. 2019b, ApJL, 870, L6
Verscharen, D., Chandran, B. D. G., Boella, E., et al. 2022, FrASS, 9, 951628
Verscharen, D., Klein, K. G., Chandran, B. D. G., et al. 2018, JPlPh, 84, 905840403
Verscharen, D., Klein, K. G., & Maruca, B. A. 2019, SoPh, 16, 5
Viñas, A. F., & Gurgiolo, C. 2009, JGRA, 114, A01105
Yoon, P. H. 2017, RvMPP, 1, 4
Yoon, P. H., Seough, J., Salem, C. S., & Klein, K. G. 2019, PhRvL, 123, 145101